

Magnetic skyrmionic structures with variable topological charges in engineered Dzyaloshinskii-Moriya interaction systems

Received: 11 October 2024

Accepted: 25 March 2025

Published online: 11 April 2025

 Check for updates

Heng Niu¹, Han Gyu Yoon², Hee Young Kwon³, Zhiyuan Cheng¹, Siqi Fu¹, Hongying Zhu¹, Bingfeng Miao¹, Liang Sun¹, Yizheng Wu⁴, Andreas K. Schmid⁵, Kai Liu⁶, Changyeon Won², Haifeng Ding¹✉ & Gong Chen¹✉

Magnetic skyrmionic structures, including magnetic skyrmions and anti-skyrmions, are characterized by swirling spin textures with non-trivial topologies. They are featured with specific topological charges, Q , which are of crucial importance in determining their topological properties. Owing to the invariance of the chiral nature, it is generally believed that Q is conserved in a given magnetic skyrmionic structure and is hard to alter. Here, we experimentally realize the control of Q of magnetic skyrmionic structures at room temperature in a Dzyaloshinskii-Moriya interaction (DMI) platform with spatially alternating signs. Depending on how many times it crosses the interfaces between DMI regions with opposite signs, the magnetic skyrmionic structures possess different Q . Modifying the DMI energy landscape through chemisorbed oxygen, a magnetic topological transition is realized. This creation and manipulation of magnetic skyrmionic structures with controllable Q , in particular the DMI-stabilized thin-film antiskyrmions and high- Q skyrmionic structures, enables a new degree of freedom to control their dynamics via a novel DMI confinement effect. Our findings open up an unexplored avenue on various topological magnetic skyrmionic structures and their potential applications.

Magnetic skyrmionic structures, e.g., magnetic skyrmions, carry specific topological charges due to their unique spin textures^{1–3}, where the spins of a magnetic skyrmionic structure wrap around the surface of a sphere, resulting in an integer topological charge, Q ⁴. In the case of magnetic skyrmion, Q is either +1 or –1 as spins wrap once around the sphere⁵. The topological charge on magnetic skyrmions gives rise to fascinating topological properties, such as the topological Hall effect⁶, skyrmion Hall effect^{7,8}, or finite topological protections^{9,10}. Their size can be extremely small, down to a few nm, and they can behave as

quasiparticles, which may allow magnetic skyrmions to propagate while dodging defects without significant pinning under external stimuli¹¹. Owing to these unique properties, magnetic skyrmions are considered to be application-relevant and promising for future spintronics applications^{12,13}.

Exploring magnetic textures with different topological charges is of great interest because of their rich topology-governed properties¹⁴. These chiral textures are typically stabilized by the Dzyaloshinskii-Moriya interaction (DMI)^{15,16}, which arises from the inversion symmetry

¹National Laboratory of Solid State Microstructures, Department of Physics and Collaborative Innovation Center of Advanced Microstructures, Nanjing University, Nanjing, People's Republic of China. ²Department of Physics, Kyung Hee University, Seoul, South Korea. ³Center for Semiconductor Technology, Korea Institute of Science and Technology, Seoul, South Korea. ⁴Department of Physics, State Key Laboratory of Surface Physics and Advanced Materials Laboratory, Fudan University, Shanghai, China. ⁵NCEM, Molecular Foundry, Lawrence Berkeley National Laboratory, Berkeley, CA, USA. ⁶Physics Department, Georgetown University, Washington, DC, USA. ✉e-mail: hfding@nju.edu.cn; gch@nju.edu.cn

breaking of the system. Magnetic textures that carry different topological charges have been found in various systems; for example, antiskyrmions have been found in anisotropic DMI systems^{17,18}, which exhibit $|Q|=1$, but Q is opposite to the skyrmion case with the same polarity. Topological charge $|Q|$ can also be different than 1, e.g., magnetic meron structures with $|Q|=0.5$ ¹⁹, fractional skyrmion lattice in anisotropy-tuned systems^{20,21}, Skyrmion-lattice-like structures with high- Q in frustrated systems²², target skyrmions²³, or skyrmion bag structures where multiple skyrmions are captured in ring-like domains²⁴.

Controlling the topological charge of an individual skyrmion is fundamentally interesting and application-relevant. In general, the DMI can set the chirality in skyrmions^{25,26}. The stabilization of anti-skyrmions in thin-film DMI systems, however, remains unattainable since the crystal symmetries, such as S_4 and D_{2d} , that support anisotropic DMI are exclusive to bulk materials. Moreover, stabilizing $|Q| > 1$ in individual magnetic skyrmionic structures is mathematically forbidden in homogenous DMI systems²⁷, as the DMI energy cannot change its sign more than four times along one circle, limited by the symmetry of the DMI energy term (see details in Fig. 1). It's worth noting a few exceptions: kink-skyrmions can emerge in a DMI system possessing high- Q , where its Q is determined by the number of kinks^{28,29}. In dipole-dominated systems without DMI, perpendicularly magnetized bubble-like domains may carry various Q numbers^{30,31}. However, the Q numbers of these skyrmionic structures are essentially uncontrolled, due to the achiral nature of the dipole interaction³².

In this article, we report the realization of well-controlled topological charges in individual magnetic skyrmionic structures via interfacial DMI engineering in a $[\text{Ni}/\text{Co}]_n/\text{Pd}/\text{W}(110)$ system. A key feature of this system is that it provides the possibility to create a landscape of two types of regions with opposite signs of the DMI. As a result, the chirality along the boundary of an individual magnetic

skyrmionic structure can vary its handedness back and forth when passing through boundaries between DMI regions with opposite signs. In these experiments, we determine the detailed inner structures of the magnetic skyrmionic structures by 3D magnetization vector imaging using spin-polarized low-energy electron microscopy (SPLEEM)^{33,34}. In particular, we find that DMI-stabilized antiskyrmions can be realized when skyrmionic structures cross the boundaries between DMI regions with alternating sign twice, and high- Q skyrmionic structures are observed when such crossing occurs more than two times. We also experimentally demonstrate the switching of Q in an individual magnetic skyrmionic structure by adjusting the DMI energy landscape. Further, we use micromagnetic simulations to demonstrate how such systems with spatially alternating DMI sign open new degrees of freedom for spin dynamics in the current-driven dynamics of magnetic skyrmionic structures.

Results

First, we discuss the possible spin structures of individual magnetic skyrmionic structures that have topological charge Q , where Q is mathematically defined as $Q = \frac{1}{4\pi} \iint \mathbf{m} \cdot \left(\frac{\partial \mathbf{m}}{\partial x} \times \frac{\partial \mathbf{m}}{\partial y} \right) d^2 \mathbf{r}$ ^{4,5}, where \mathbf{m} is the spatially dependent magnetization. In this article, we focus on perpendicularly magnetized systems with thicknesses well below the formation of closure domains³⁵, and one can assume that the spins along the z -direction are uniform; therefore, the determination of Q of magnetic skyrmionic structures can be simplified into mapping the in-plane spin components at the boundaries of magnetic skyrmionic structures^{4,5}, e.g., obtaining Q via counting the accumulative magnetization rotation angle in two dimensions⁵.

Unity charge $Q = \pm 1$ requires a 2π accumulative rotation of the in-plane magnetization. It often results in skyrmions observed in systems featuring the various DMI types, e.g., Bloch-type chirality governed by the bulk-DMI (Fig. 1a, d)^{1,2,25}, Néel-type chirality governed by the

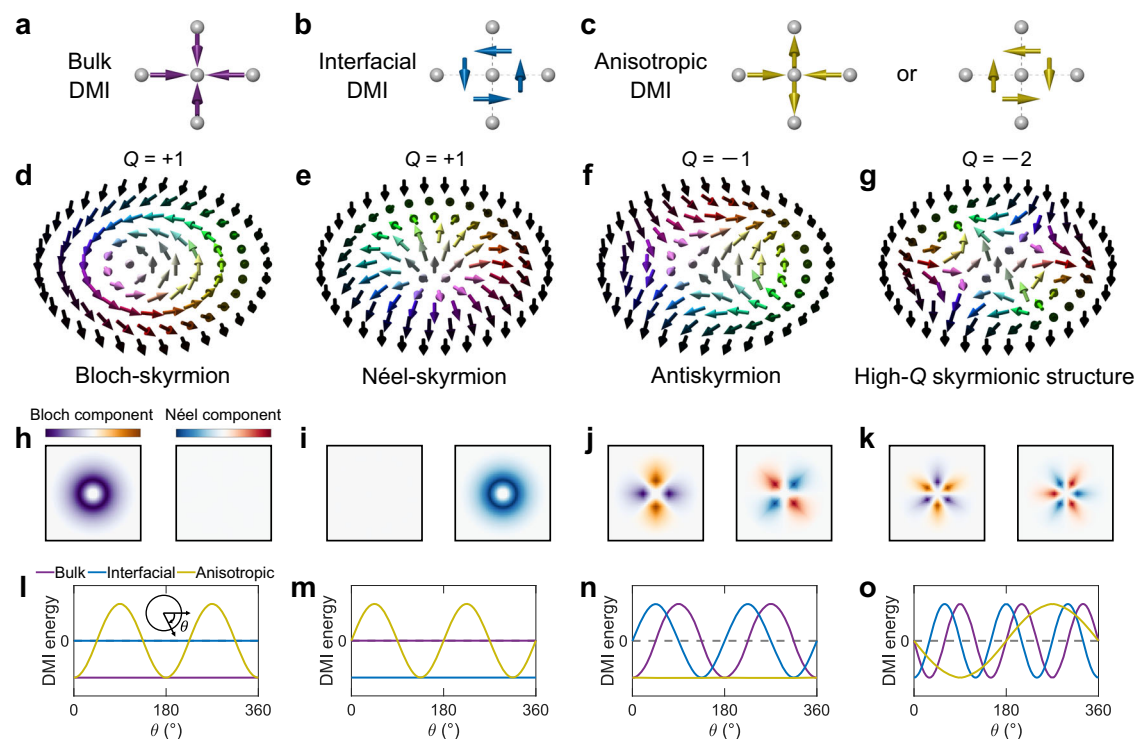


Fig. 1 | DMI energies of various magnetic skyrmionic structures in systems with different types of DMI. **a–c** Sketch of the bulk, interfacial, and anisotropic DMI, respectively. The arrows present the direction of the local DMI vector. **d–g** Magnetic moment vector representation of Bloch-type skyrmion, Néel-type skyrmion, Antiskyrmion, and High- Q skyrmionic structure, respectively. **h–k** Top

view of the Néel- and Bloch-component of the DMI energy distribution within magnetic skyrmionic structures. **l–o** Azimuthal-angle-dependent DMI energy density of the corresponding spin textures in **(d–g)** in the case of bulk-, interfacial, and anisotropic DMI.

interfacial-DMI (Fig. 1b, e)^{3,26}, and anisotropic chirality induced by anisotropic-DMI (Fig. 1c, f)^{17,18}. In these systems, the DMI vectors align differently with respect to the distance vectors between pairs of nearest-neighbor atoms, because of the distinct crystalline symmetries. For example, the bulk-DMI-vectors are parallel to the distance vectors with the same sign (Fig. 1a)^{2,25}, the interfacial-DMI-vectors are perpendicular to the distance vectors with the same sign (Fig. 1b)^{3,26}, anisotropic-DMI-vectors could be either parallel or perpendicular to the distance vectors but with opposite signs (Fig. 1c and Methods)¹⁷.

In the following, we show how magnetic skyrmions carrying $Q = \pm 1$ can be shaped by the DMI types mentioned above, and we discuss why magnetic skyrmions with $|Q| > 1$ cannot be stabilized in a homogenous DMI system based on DMI energies. The spin textures of Bloch-skyrmion², Néel-skyrmion³, antiskyrmion¹⁷ and a high- Q skyrmionic structure³¹ are illustrated by magnetic moment vector plots (Fig. 1d–g), where the corresponding Q of +1, +1, -1 and -2 are marked above the sketches, and the maps of their decomposed Bloch-/Néel-components are highlighted in Fig. 1h–k. For each type, the azimuthal angle-dependent variations of the DMI energies are presented in Fig. 1l–o, i.e., the DMI variation for the Bloch-type skyrmion shows that the bulk-DMI remains the lowest energy type among all (Fig. 1l). One can also note that the angle-dependent energy costs for interfacial-DMI/anisotropic-DMI remain the lowest for the Néel-skyrmion/antiskyrmion (Fig. 1m, n), respectively. However, for a high- Q skyrmionic structure (Fig. 1g), the azimuthal angular dependence of the DMI energies oscillates around 0 in all three DMI types (Fig. 1o), because of the three-fold symmetry of the alternating Bloch-/Néel-chiralities (Fig. 1k). Thus, none of DMI type can stabilize a high- Q skyrmionic structure with $|Q| > 1$.

One way to break the fundamental limit of the DMI stabilized magnetic skyrmionic structures with a high Q number is to chop the magnetic chirality and reassemble them with alternating DMI sign (Fig. 2a). In multilayer films, the sign and the strength of the DMI can be tailored by adjusting the thickness of the heavy metal layer³⁶, which allows one to control the DMI sign with various film thicknesses locally. We chose the [Ni/Co]_n/Pd-multilayers grown on W(110) through molecular beam epitaxy (MBE) because it features a Pd-thickness-dependent DMI sign transition, and because the growth of Pd at elevated temperature results in large areas of homogeneous thickness³⁷. The latter enables the preparation of surfaces with separated DMI regions, where the thicker (thinner) Pd region favors the left (right)-handed chirality³⁶. In the experiments, these regions of different Pd thickness, e.g., 1 monolayer (ML) or 0 ML, are identified by their significant difference in LEEM image brightness³⁸ (Fig. 2b and Methods), and the lateral sizes of these regions could be well controlled by changing the growth temperature of Pd (Fig. S2 and Methods). Additional Pd with an effective thickness of 1.9 ML is grown at room temperature, transforming the surface from the regions with 1 ML Pd and 0 ML Pd to the regions with 2.9 ML Pd and 1.9 ML Pd. Note that room-temperature-grown non-integer monolayers form islands that are unresolvable within the lateral resolution of LEEM (~7 nm) and are also much smaller than the spin structures observed here. Therefore, the role of non-integer Pd thickness in domain structures can be considered as an averaging effect on the magnetic parameters. When [Ni (2.1 ML)/Co (1 ML)]₂ films are grown on such Pd/W(110) surfaces, then perpendicularly magnetized domains form where magnetic domain boundaries may go across regions with alternating Pd thicknesses, resulting in non-homo-chiral-like features within the domain wall's magnetization (Fig. 2c). The thickness of [Ni/Co]_n multilayers is optimized to acquire the uniform perpendicular magnetized domains. To visualize the role of the DMI region with alternating sign, the Néel-components of the domain walls are derived (Methods) and represented in a color scale, which is superimposed on the LEEM image highlighting various Pd thickness regions (Fig. 2d). It shows a clear modulation of the chirality sign synchronized with the Pd thicknesses

variation, where the chirality/DMI signs change and Pd thickness regions match perfectly. This effect is further verified by Monte-Carlo simulations (Methods), with the pre-defined DMI regions following the Pd morphology of the LEEM data in Fig. 2b, successfully reproducing the experimental observation (Fig. 2e).

We notice that such a DMI modulation effect is dependent on the total length of the domain wall (DW) within a region of the same DMI sign (Fig. S3a–h), e.g., while the modulation of the Néel-component works when the length of DW in the same sign DMI region (corresponding to L_{DW}) is above ~100 nm (the dashed line in Fig. 2f). The Néel-components might not flip its chirality when the length of DW in the same sign DMI region is down to tens of nm or less (Fig. S3). This is attributed to the interplay between the exchange interaction and the DMI, i.e., the spins at the boundary between two Néel-components with opposite chirality need to rotate by 180°, lifting the energy cost of the exchange interaction, which may prevent the chirality flipping on a given area if DW's length is too short within a uniform DMI region. We define the angle α as the deviation angle of measured magnetization in DW from magnetization in expected Néel DW. We experimentally count the dependence of α on L_{DW} (Fig. 2f). The results indicate that as the length of DW in uniform DMI region shortens, the deviation angle increases. The difference between the two DMI regions is relevant to the Pd-thickness-dependent DMI variation in the Co/Pd/W(110) system³⁶, where 1 ML Pd thickness difference induces $\Delta\text{DMI} \approx 0.41 \pm 0.17$ meV/atom. To flip the chirality of a DW in a shorter length, one would need a substantially stronger DMI difference. To simplify the model and simulation, we set the DMI-reversal line crossings always to be perpendicular to the DW, which means that the width of uniform DMI region w_{DMI} is equal to the length of DW L_{DW} in it (Fig. S3i). This relation is quantitatively simulated in the $L_{\text{DW}} - D_{ij}$ phase diagram (Fig. 2g). Furthermore, we developed an analytical model of the spin configurations in domain wall structures with alternating DMI (Fig. S4 and Note S1). In it, we define a critical length of DW in the same sign DMI region $L_{\text{DW,c}}$ where the transition between the alternating Néel domain wall and the uniform Bloch domain wall occurs, and estimate it to be,

$$L_{\text{DW,c}} \sim \frac{\lambda_{\text{Dip}}}{\lambda_{\text{Dip}} - \lambda_{\text{DM}}} \sqrt{\lambda_{\text{K}} \lambda_{\text{DM}}} \quad (1)$$

where the λ_{Dip} , λ_{K} , and λ_{DM} represent the length scale of dipole interaction, magnetic anisotropy, and interfacial DMI, respectively (Details in Note S1). The result of the analytical model is denoted by an orange dashed line in Fig. 2g, which agrees well with the results of the Monte-Carlo simulations.

Next, the role of the DMI modulation on skyrmions' spin textures is explored using Monte-Carlo simulation, and the parameters are chosen to enable Néel-chirality to be successfully flipped (Methods). We define n as the number of DMI-reversal line crossings (number of DMI reversals). When $n = 0$, namely in a uniform DMI system, a Néel skyrmion with $Q = 1$ (Fig. 3a, b) is formed due to the interfacial DMI. In the case of $n = 1$, as compared to the $n = 0$ case (Fig. 3a), it adds a DMI area with the opposite sign on the right (Fig. 3c). Consequently, it cuts the ring-like domain wall into two segments with opposite chirality. Note that Bloch components also form at locations where the opposite-chirality segments meet. Thus, the spins in the domain walls point in the same direction (Fig. 3d), forming a topological-trivial bubble with $Q = 0$. In the $n = 2$ case, there is another DMI area with the opposite sign added on the right. This creates a new cut on the domain wall, and it breaks into four pieces with alternating Néel-chirality (Fig. 3e). Thus, an antiskyrmion with $Q = -1$ is stabilized (Fig. 3f). Similarly when n increases to 3, the domain wall of the bubble has six pieces with alternating Néel-chirality (Fig. 3g) and a magnetic skyrmionic structure with $Q = -2$ forms (Fig. 3h). We performed simulations with further increasing n and find magnetic skyrmionic structures with

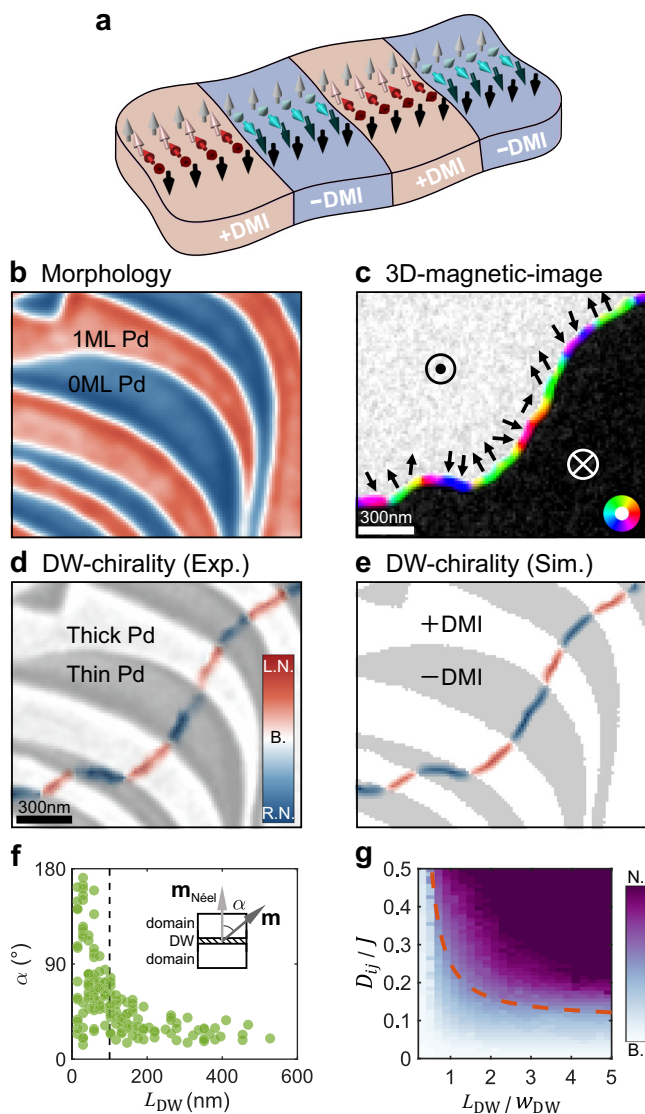


Fig. 2 | DMI modulation on the engineered surfaces. **a** Sketch of the local chirality control via an inhomogeneous surface. **b** LEEM image of the morphology of Pd stripes grown on W(110) surface; 1 ML and 0 ML Pd regions are shown in red and blue, respectively (imaging condition: 1.5 eV). **c** Compound SPLEEM image of perpendicularly magnetized domain structures of $[\text{Ni}(2.1 \text{ ML})/\text{Co}(1 \text{ ML})_2$ grown on the Pd stripes with alternating thickness of 1.9 ML and 2.9 ML on W(110) substrate (Method), where the black arrows and the color wheel highlight the spin inside the domain walls. **d** Derived Néel-chirality within the domain walls is highlighted by the thin, colorized lines, which are superimposed onto the LEEM image of Pd film thickness in **(b)**. L.N., B., and R.N. stand for the left-handed Néel, Bloch, and right-handed Néel, respectively. **e** Simulated domain walls' Néel-chirality on surfaces with DMI regions with opposite signs, input by **b**. Positive DMI corresponds to left-handed chirality. **f** Experimental statistics on the dependence of α on L_{DW} . The inset is a schematic diagram defining α . \mathbf{m} is the measured magnetization unit vector. $\mathbf{m}^{\text{Néel}}$ is the expected magnetization unit vector in Néel DW controlled by engineered-DMI. L_{DW} is the length of DW within the DMI region of the same sign. **g** Monte-Carlo simulated phase diagram in $L_{\text{DW}} - D_{ij}$ space, where w_{DW} is the width of the domain wall, J is the strength of symmetric exchange interaction, and D_{ij} is the strength of the DMI. The strength of the Bloch/Néel component is defined by the color bar. The orange dashed line represents the result of the analytical model of the boundary between alternating Néel domain walls and uniform Bloch domain walls.

$Q = 1 - n$ can be stabilized, e.g., $Q = -3, -4, -5$ (Fig. S5). The relationship between Q and n follows $Q = 1 - n$ (Fig. 3i), indicating that the topological charge of the magnetic skyrmionic structures could be well-tuned through DMI engineering (Details in Note S2). In addition, the sign of Q depends on the polarity of the core of the bubble ($Q = n - 1$ in the opposite polarity case). To ensure that the DMI is always able to control the Néel chirality on the bubble boundary, the length of DW in the DMI region of the same sign cannot be too short (as discussed above), which makes the size of the stabilized skyrmionic structure of higher topological charge necessarily larger³¹. However, the size of skyrmionic structures cannot be too large. This is due to the fact that the energy difference between different Q states with the same n is dependent on their size. When the skyrmionic structure is too large, the spin inside the Bloch line (BL) will rotate completely randomly, thus failing to modulate Q . The energy difference between clockwise and counter-clockwise rotational spin configurations in BL can be estimated as:

$$\Delta E_{\text{BL}} \sim J\pi \frac{\lambda_K}{R} \quad (2)$$

where the J and R represent the strength of exchange interaction and the radius of skyrmionic structures, respectively (Details in Note S3).

Further, we experimentally demonstrated that alternating DMI could modulate the topological charge of magnetic skyrmionic structures. Here we only count the effective DMI-reversal line crossings (the length of DW in the DMI regions of the same sign is well above 100 nm). The topological charges of experimentally observed magnetic skyrmionic structures are determined through accumulative magnetization rotation around the object's boundary, as described in ref. 39 (Fig. S8). A left-handed Néel skyrmion is captured on the thinner-Pd region (Fig. 3j, k). When half of the bubble lands on the Pd stripe ($n=1$), it forms a topological-trivial bubble (Fig. 3l, m). The derived Néel-component image superimposed on the LEEM image with different Pd thickness regions shows that DMI modulates the chirality sign of bubble wall (Fig. 3l). When the entire Pd stripe crosses a single bubble, resulting in $n=2$ crossings, the Néel-chiralities parallel and perpendicular to the Pd-stripe are opposite, resulting an anti-skyrmion which is clearly observed by SPLEEM (Fig. 3n, o). More Pd stripes going through the bubble lead to a higher topology charge ($n=3$, resulting in $Q=-2$ in Fig. 3p, q). To the best of our knowledge, this is the first experimental observation of anti-skyrmions and high- Q skyrmionic structures in an interfacial DMI system. The more explicit criteria for counting crossing events in the experiments are shown in Fig. S9. The Néel-components do not flip their chirality when the length of DW in the same DMI sign region is too short, as discussed above. We've statistically counted the effective DMI-reversal line crossing events, and the experimental dependence of Q on n_{eff} is summarized in Fig. 3r. The topological charge Q deviates from theoretical expectations in large skyrmionic structure cases. We attribute such deviation to the skyrmionic structures' size-dependent Q expectation (discussed in Note S3), as well as the irregular shape of the skyrmionic structures.

The transformation between magnetic skyrmionic structures with different topological charges is appealing from the topological magnetism point of view^{14,40}. In future spintronic devices, encoding data using the topological degree of skyrmionic structures can increase storage density to achieve multiple-valued memory²⁴. Being able to alter the topological charges of skyrmionic structures extends the freedom of the racetrack memory or computing devices⁴¹. There are currently several ways to trigger topological transitions: external magnetic field can be applied to forcibly switch the in-plane component in magnetic skyrmions^{42,43} and merons¹⁹, thereby realizing metastable topological transitions. Magnetic topological transitions can also be achieved by using electrical current⁴⁴, ultrafast laser excitation⁴⁵, and chemical-pressure-controlled method⁴⁶.

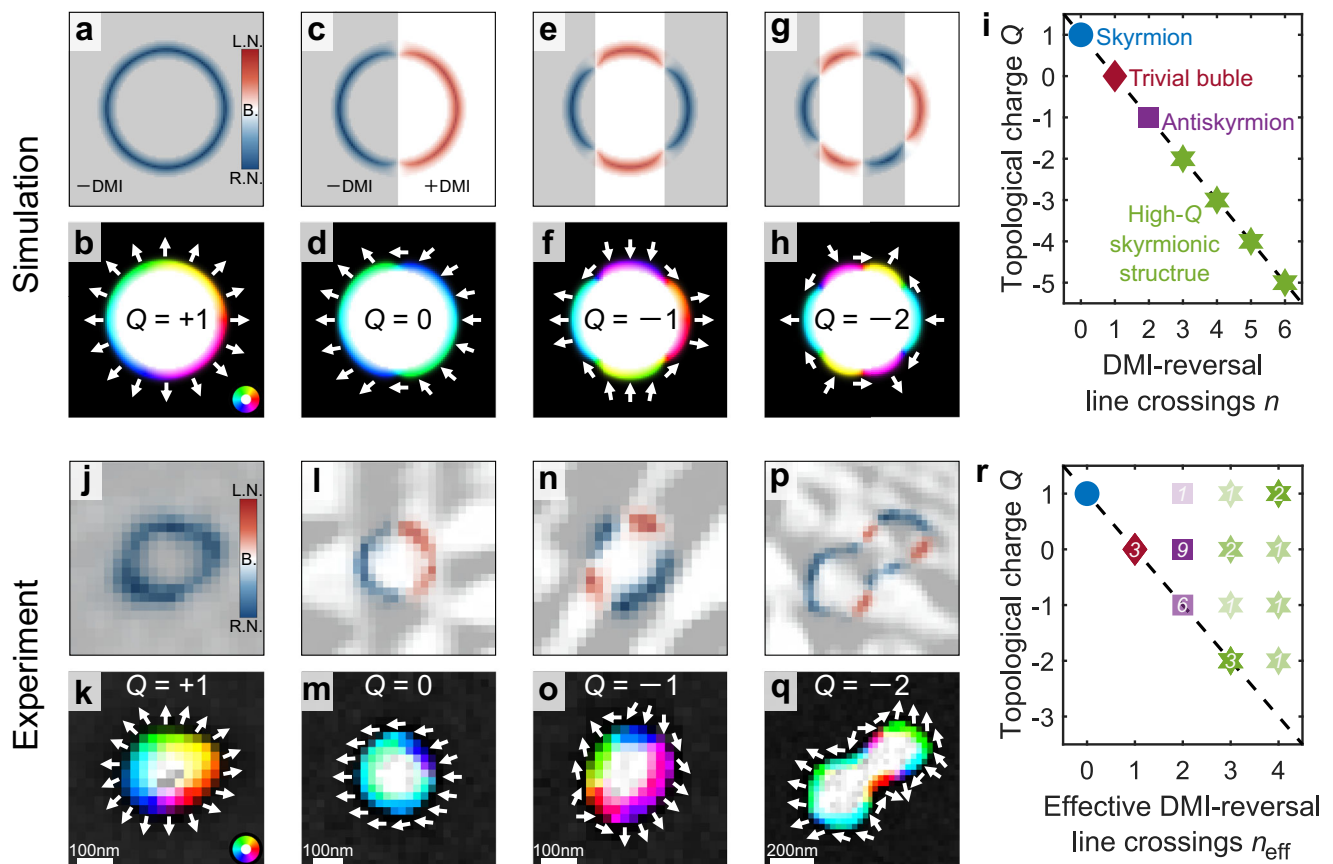


Fig. 3 | Tailoring topological charge of magnetic skyrmionic structures via DMI engineering. **a–h** Monte-Carlo simulations of skyrmionic structures with topological charge equals +1, 0, -1, -2 through DMI-reversal line crossing 0, 1, 2, 3 times, correspondingly. The DMI's sign settings in the simulation are indicated by the light and dark in the derived Néel-chirality image. **i** Dependence of Q on the DMI-reversal line crossing n in Monte-Carlo simulations. **j–q** Derived Néel-chirality images

overlapped with the morphology LEEM images and corresponding compound SPLEEM images of skyrmion (**j, k**), trivial bubble (**l, m**), antiskyrmion (**n, o**), and high- Q skyrmionic structure (**p, q**) in [2 ML Ni/1 ML Co]₂/2 ML & 3 ML Pd/W(110). **r** Experimental statistics on the dependence of Q on the effective DMI-reversal line crossing n_{eff} . The numbers on the scatters indicate the number of events observed in the experiment for each case.

In the following, we demonstrate how topology transitions between stable magnetic skyrmionic structures can be induced by experimentally altering the DMI landscape. Utilizing the oxygen-coverage-dependent DMI transition at the oxygen/Ni interface described in ref. 36 (Methods), we flipped the areas with left-handed DMI in the [Ni/Co]_n/Pd/W(110) system to right-handed DMI in the O/[Ni/Co]_n/Pd/W(110) system, thereby transforming the alternating-DMI system into a homogeneous DMI system. As a result, the transformations of a trivial bubble and an antiskyrmion into skyrmions are experimentally realized, respectively (Fig. 4a–d, e–h). This topological transition triggered by flipping the DMI energy landscape is further examined through Monte-Carlo simulations (Methods), where we find that a trivial bubble is transformed into a skyrmion (Fig. 4i–l), and an antiskyrmion is converted to a skyrmion (Fig. 4m–p), which agrees well with experiments. The ability to alter the topological charge of magnetic skyrmionic structures through altering the DMI could be further extended to magneto-ionic devices^{47,48}, where electrical signals permit tuning of the DMI at solid interfaces.

Various magnetic skyrmionic structures, e.g., antiskyrmions¹⁷, skyrmion bags²⁴, chiral bobbars⁴⁹, etc., are considered potential information carriers for next-generation magnetic memories, and their current-driven dynamics on the racetrack are of intense interest^{11,14}. We have carried out micromagnetic simulations to study the dynamics of skyrmions, antiskyrmions, and high- Q skyrmionic structures on alternating-DMI racetracks in which the sign of DMI at the central

region is opposite to that in the two side regions (Methods). First, a left-handed Néel skyrmion (supported by positive-DMI) is trapped by two negative-DMI regions (Fig. 5a). The skyrmion, driven by spin-transfer-torque, moves along the racetrack with suppressed skyrmion Hall effect (Supplementary Video 1). The DMI regions of the opposite sign at the two sides exert a repulsive effect on the skyrmion, thus restricting the skyrmion to always be near the central position of the racetrack. A similar repulsive effect on skyrmions between DMI and zero-DMI regions has also been reported in ref. 50.

Then, an antiskyrmion is introduced on the racetrack. Due to the twofold symmetry of chirality of the antiskyrmion (Fig. 1g), it is riding on the positive-DMI stripe while keeping the other two sides located on the negative-DMI region (Fig. 5b). This property allows one-dimensional motion of antiskyrmion when driven by current (Supplementary Video 2). Furthermore, skyrmion and antiskyrmion chains could be driven on the same racetrack with an alternating-DMI landscape (Supplementary Video 3). With racetracks partitioned into more regions of alternating DMI (Fig. 5c), high- Q skyrmionic structures can also be driven along the racetrack, with suppressed skyrmion Hall effect (Supplementary Video 4). More intriguingly, skyrmions, antiskyrmions, and high- Q skyrmionic structures can all be encoded into one racetrack and driven by current simultaneously with essentially the same speed v (Supplementary Video 5), casting a strong potential in multi-state racetrack memory application. We studied v of skyrmionic structures with different Q driven by different current

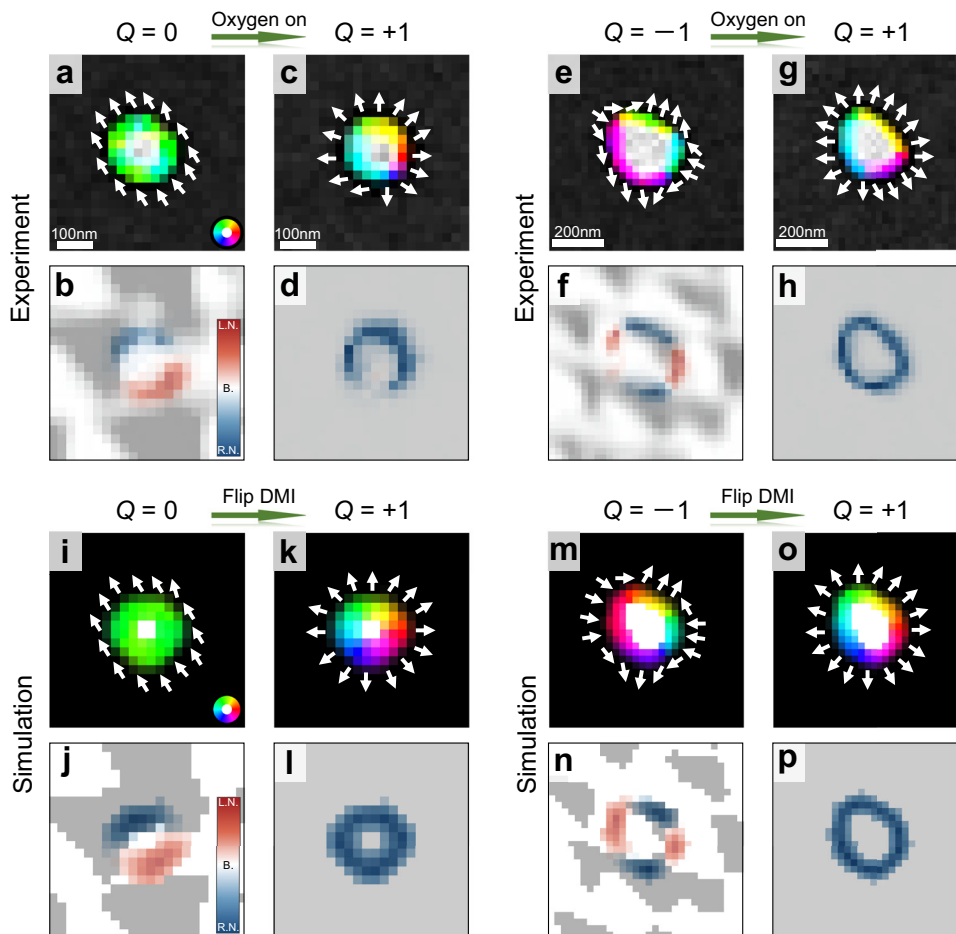


Fig. 4 | Topological transitions of magnetic skyrmionic structures induced by gas adsorption. **a** Compound SPLEEM image of a trivial bubble in the alternating-DMI system $[\text{Ni}/\text{Co}]_n/\text{Pd}/\text{W}(110)$. **b** The corresponding Néel-chirality image overlaid with the morphology image. **c, d** compound SPLEEM image and derived Néel-chirality image at the same location after -0.2 ML oxygen chemisorption.

e-h Compound SPLEEM image and Néel-chirality image overlaid with morphology image of antiskyrmion transformed into skyrmion. **i-l, m-p** Monte-Carlo simulations of topological transition of trivial bubble and antiskyrmion to skyrmions, respectively. The DMI's initial sign settings in the simulation are adapted from experimental LEEM images, indicated by the light and dark in **(j, n)**.

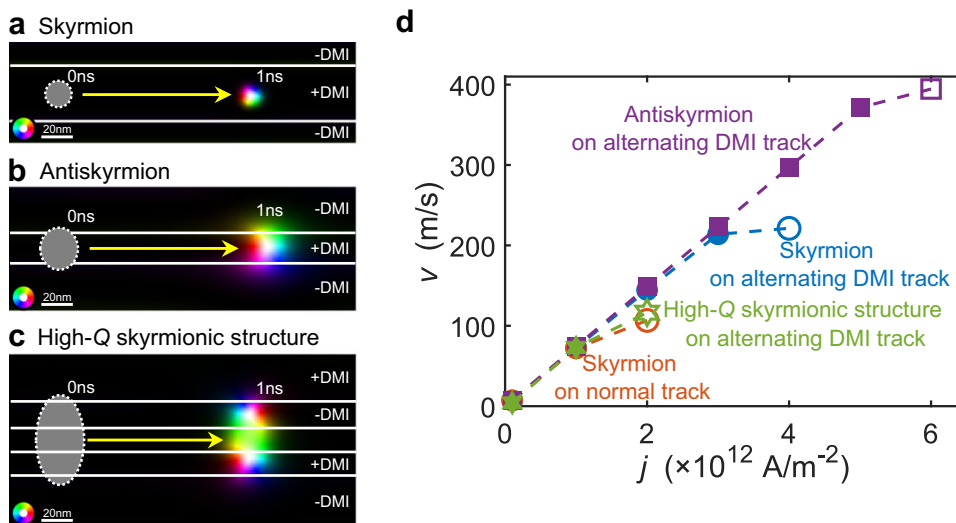


Fig. 5 | Current-driven motion of various magnetic skyrmionic structures on the racetrack without the skyrmion Hall effect. **a-c** Spin-transfer-torque drives the skyrmion **(a)**, antiskyrmion **(b)**, and high-Q skyrmionic structure **(c)** to move along the DMI-engineered racetrack. The dotted line marks the initial position of

the magnetic skyrmionic structures. **d** Various skyrmionic structures' velocity v as a function of electrical current density j . The empty symbols mean that the skyrmionic structures will annihilate at the present current density.

densities j as summarized in Fig. 5d. For skyrmions, the critical current density of the annihilation, when pushed to the DMI boundary, is larger compared to when being pushed to the physical boundary (Blue and orange circles in Fig. 5d). Notably, the antiskyrmion on the engineered-DMI-racetrack can move at speeds up to 370 m/s (Purple squares in Fig. 5d).

Discussion

The number of the topological charge Q is typically ± 1 for skyrmions or antiskyrmions. As discussed earlier, $|Q|$ within a single magnetic skyrmion cannot be greater than 1 in a system with homogeneous DMI. The high- Q ($|Q| > 1$) skyrmionic structure opens up new opportunities for topological magnetism as there is rich physics related to the topological charge, such as skyrmion Hall effect^{7,8,31}, or topological Hall effect⁶. Note that engineering laterally varying DMI structures is not limited to the $[\text{Ni}/\text{Co}]_n/\text{Pd}/\text{W}(110)$ system, but can be realized in other metal multilayers, with either thickness-dependent competing DMI³⁶, local modification of the DMI at the interface^{51,52}, electric field tuned DMI⁵³, strain manipulated DMI⁵⁴ and band-filling control of DMI in weakly ferromagnetic insulators⁵⁵. As shown in Figs. 2f and S3, the chirality may not flip as designed in an engineered-DMI system. It is due to the short DW length in the narrow DMI region of the same sign or some pinning defects caused by inhomogeneous Pd layers⁵⁶. Further enhancing the strength of engineered-DMI can achieve better control of chirality according to Fig. 2g. Advanced patterning of the DMI energy landscape and precise control over the size of the skyrmionic structures will enable more accurate regulation of Q .

In our simulation, the skyrmions ($Q = 1$), antiskyrmions ($Q = -1$), and high- Q skyrmionic structures ($Q = -2$) are driven by spin transfer torque along the DMI-engineered racetrack. The role of spin-orbit torque (SOT) on antiskyrmions and high- Q skyrmionic structures is usually not considered due to the presence of opposite chirality in their structures^{31,57}. We simulate SOT-dynamics on a racetrack in which DMI and spin Hall angle (SHA) are simultaneously altered and find skyrmions, antiskyrmions, and high- Q skyrmionic structures moving along the racetrack with suppressed skyrmion Hall effect (Fig. S10 and Methods). The DMI- and SHA-engineered racetrack can be realized in bilayer systems such as Pd (positive DMI, positive SHA)/W (negative DMI, negative SHA) and Ir (negative DMI, positive SHA)/Ta (positive DMI, negative SHA)⁵⁸. Besides the potential memory application, stabilizing magnetic skyrmionic structures with controllable Q also provides a platform for exploring Q -relevant topological properties, e.g., topological stability^{9,10}. It indicates the possible potential for the Q -based quantum computation⁵⁹. Moreover, a magnetic skyrmion of an even azimuthal winding number placed in proximity to an s -wave superconductor can induce a zero-energy Majorana-bound state in its core theoretically⁶⁰. Related to that, isolated nano-skyrmions were observed in the Co/Ru(0001) system. Ru turns superconductive below 0.5 K⁶¹, and we anticipate that utilizing the Co/Pd/Ru(0001) system will enable tuning the topological charge of magnetic skyrmionic structures to an even number, which may induce a zero-energy Majorana-bound state in the core of such even- Q skyrmionic structures.

In summary, we have successfully controlled the Néel-chirality of domain walls and the topological charge of magnetic skyrmionic structures through DMI engineering in the $[\text{Ni}/\text{Co}]_n/\text{Pd}/\text{W}(110)$ system. The results have been verified by LEEM/SPLLEEM imaging and Monte-Carlo simulations. By changing the DMI energy landscape of the whole system, transitions from trivial bubbles and antiskyrmions to skyrmions are demonstrated. Using micromagnetic simulations, the current-driven motion of various magnetic skyrmionic structures on the DMI-engineered racetrack with suppression of the skyrmion Hall effect is achieved. Our findings of tunable topological charge of magnetic skyrmionic structures based on the DMI engineering further open up new vistas for topology in magnetism.

Methods

Anisotropic DMI matrix transformation

The anisotropic DMI matrix in 2D system can be written as:

$$\mathcal{D} = \begin{pmatrix} D & 0 \\ 0 & -D \end{pmatrix} \quad (3)$$

The operation matrix of rotating θ angle along the z -axis in 2D system can be written as:

$$R_z(\theta) = \begin{pmatrix} \cos \theta & -\sin \theta \\ \sin \theta & \cos \theta \end{pmatrix} \quad (4)$$

Under the operation of rotating 45° along the z -axis the anisotropic DMI matrix is transformed to

$$\mathcal{D}' = \det(R_z(45^\circ)) R_z(45^\circ) \mathcal{D} R_z(45^\circ)^{-1} = \begin{pmatrix} 0 & D \\ D & 0 \end{pmatrix} \quad (5)$$

Sample preparation

The experiments were performed on Elmitec SPLLEEM III at the National Laboratory of Solid State Microstructures and the Department of Physics at Nanjing University. To clean the W(110) substrate, cycles of flashing to 1850 °C were done in an oxygen background at 3×10^{-8} Torr until the surface was free of carbon, confirmed by Auger electron spectroscopy (AES), low-energy electron diffraction (LEED), and low-energy electron microscopy (LEEM). Additional flashing removes the adsorbed oxygen from the surface. Pd, Co, and Ni layers were deposited by molecular beam epitaxy (MBE) in the SPLLEEM chamber under ultra-high vacuum (UHV) with a base pressure of 4×10^{-11} Torr. The pressure was around 5×10^{-10} Torr at the time of growth. The film thicknesses were calibrated via oscillations of the LEEM intensity (grow Co, Ni, Pd at room temperature with -1.5 eV imaging electron energy) and via directly visible step-flow growth in-situ LEEM at elevated temperature (Co, Ni growth at 400 °C and Pd at 700 °C on W(110) with -5 eV imaging electron energy).

To prepare the DMI-engineered surfaces, we first grow Pd on W(110) in the range of 0.3–0.7 ML at 700 °C. This leaves 30–70% of the surface area covered with 1 ML Pd, and the rest of the surface area is bare W(110) substrate. After cooling the sample back to room temperature, we continued to grow an additional -1.9 ML Pd, so that thicknesses of the resulting Pd film regions straddle the zero-DMI point of the $[\text{Ni}/\text{Co}]_n/\text{Pd}/\text{W}(110)$ system when the Pd thickness is -2.4 ML³⁶. At this point, 30–70% of the surface area is covered with -1.9 ML Pd (negative-DMI, right-handed chirality), and the rest of the surface area is covered with -2.9 ML Pd (positive-DMI, left-handed chirality). $[\text{Ni}/\text{Co}]_n$ multilayers were deposited onto these inhomogeneous Pd-thickness surfaces at room temperature. The thickness of Ni and Co was tuned to provide perpendicular magnetic anisotropy (PMA), and the in-plane uniaxial anisotropy induced by W(110) is balanced by the opposite magnetoelastic coefficients of Ni and Co. Oxygen adsorption was done by controlled leaking of high-purity oxygen (99.999%) at a pressure 1×10^{-8} Torr. The total amount of oxygen introduced in the chamber is one Langmuir, and its coverage is calibrated by LEEM-IV measurements of the changes in the work function of Ni surface^{36,62}, which corresponds to -0.2 ML chemisorbed oxygen layer for the data in Fig. 4⁶².

Magnetic imaging, chirality analysis, and image registration

Real-space magnetic images were observed using the Elmitec SPLLEEM III. The spin-polarized electron beam was generated by photoemission from GaAs(001) activated to negative electron affinity by cycles of Cs and oxygen deposition in a “yo-yo” treatment. The magnetic contrast in SPLLEEM images represents the asymmetry of the spin-dependent

reflection, which is $A = (\text{LEEM}_{\text{up}} - \text{LEEM}_{\text{down}}) / (\text{LEEM}_{\text{up}} + \text{LEEM}_{\text{down}})$. A is proportional to $\mathbf{P} \cdot \mathbf{M}$ where \mathbf{P} is the spin polarization of the incident electrons (-27% in the instrument), and \mathbf{M} is the surface magnetization of the sample. To optimize the magnetic contrast, the incident electron energy was set to 2 eV, and all SPLEEM images were measured at room temperature. The M_x , M_y , and M_z components of the magnetization \mathbf{M} were imaged by aligning the spin polarization of the electron beam along W[1-10], W[001], and W[110] directions, respectively. To get the colourized compound SPLEEM image, M_x and M_y components were mapped on the hue and the M_z was mapped on the lightness in the hue-saturation-lightness (HSL) color space. The magnetic domains and domain walls are mapped separately to maintain low noise levels.

The analysis of Néel-chirality/Bloch-chirality from SPLEEM images or simulated images was done in the following steps. First, the angles between the domain wall normal direction vector \mathbf{n} or tangential direction vector \mathbf{t} located at the center line of the domain wall and the unit direction vector \mathbf{e}_x (pointing from spin-down to spin-up domains) were calculated pixel-by-pixel:

$$\mathbf{n} \cdot \mathbf{e}_x = \tan^{-1} \left(\frac{\partial M_z / \partial y}{\partial M_z / \partial x} \right) \quad (6)$$

$$\mathbf{t} \cdot \mathbf{e}_x = \tan^{-1} \left(\frac{\partial M_z / \partial x}{\partial M_z / \partial y} \right) \quad (7)$$

Then, the angle between in-plane magnetization direction \mathbf{m} and the unit direction vector \mathbf{e}_x was determined pixel-by-pixel through:

$$\mathbf{m} \cdot \mathbf{e}_x = \tan^{-1} \left(M_y / M_x \right) \quad (8)$$

Néel-chirality or Bloch-chirality was defined from the angle between the magnetization direction \mathbf{m} being parallel to the geometric normal to the domain wall direction \mathbf{n} , or parallel to the domain wall direction \mathbf{t} , respectively. To better characterize the global chirality of in-plane magnetic domain walls in the PMA system, we multiply the angle by a factor that additionally describes the proportion of in-plane components. Finally, we calculated the strength of Néel-chirality N and Bloch-chirality B for every pixel on the SPLEEM images or the simulated images through:

$$N = (\mathbf{m} - \mathbf{n}) \cdot \mathbf{e}_x \frac{\pi/2 - \tan^{-1} \left(|M_z| / \sqrt{M_x^2 + M_y^2} \right)}{\pi/2} \quad (9)$$

$$B = (\mathbf{m} - \mathbf{t}) \cdot \mathbf{e}_x \frac{\pi/2 - \tan^{-1} \left(|M_z| / \sqrt{M_x^2 + M_y^2} \right)}{\pi/2} \quad (10)$$

For low-noise SPLEEM images, average images were formed from stacks of SPLEEM images acquired sequentially, after possible drift within the sequences of SPLEEM images was corrected using Matlab software based on the `normxcorr2` function. The registration between LEEM images of Pd-strips and SPLEEM images of magnetic domains/domain walls was all based on step bunches of the W(110) substrate, which were clearly resolved at all stages of sample preparation, including after Pd layer and $[\text{Ni}/\text{Co}]_n$ multilayer deposition. The statistics in Fig. 2f, analysis in Figs. S8 and S9 were obtained by extracting the boundary in LEEM and Néel-chirality images using Matlab software based on the `bwtraceboundary` function.

Monte-Carlo simulations

The Monte-Carlo simulations were carried out using a two-dimensional model⁶³, where exchange interaction, dipolar interaction, perpendicular magnetic anisotropy (PMA), and DMI are considered. The

Hamiltonian can be written as:

$$\mathcal{H} = -J \sum_{\langle i,j \rangle} \mathbf{S}_i \cdot \mathbf{S}_j - D_{\text{dip}} \sum_{i,j} \frac{3\mathbf{S}_i \cdot (\mathbf{r}_i - \mathbf{r}_j) \mathbf{S}_j \cdot (\mathbf{r}_i - \mathbf{r}_j) - \mathbf{S}_i \cdot \mathbf{S}_j |\mathbf{r}_i - \mathbf{r}_j|^2}{|\mathbf{r}_i - \mathbf{r}_j|^5} - K_z \sum_i S_{z,i}^2 - \sum_{\langle i,j \rangle} \mathbf{D}_{ij} \cdot (\mathbf{S}_i \times \mathbf{S}_j) \quad (11)$$

where \mathbf{S}_i and \mathbf{S}_j are spins located on atomic sites i and j in the two-dimensional plane, \mathbf{r}_i and \mathbf{r}_j are the position vectors of the spin blocks in sites i and j . The dimensionless parameters J , D_{dip} , K_z and \mathbf{D}_{ij} are used in simulations corresponding to exchange interaction, dipole interaction, PMA, and DMI, respectively. The engineered DMI and initial magnetic domain configuration in the simulations were loaded from the extracted Pd-stripe in LEEM images and the out-of-plane magnetic domain in SPLEEM images, respectively. The initial spins inside the domain walls were set to point up or down to break the in-plane symmetry, followed by annealing to an energetically stabilized state. The temperature in the simulations is represented by allowing spins to fluctuate according to Boltzmann statistics⁶³. For the simulation results summarized in Figs. 2e, g; S3d, h, i and 3a–h, the values $J=1$, $D_{\text{dip}}=0.1$, $K_z=0.65$ were assumed. $D_{ij}=0.20$ for the simulation results in Figs. 2e and S3d, h, i. $D_{ij}=0.15$ for simulated results of magnetic skyrmionic structures in Figs. 3a–h and S5. To simulate the $L_{\text{DW}} - D_{ij}$ phase diagram in Fig. 2g, the step size for the width of uniform DMI is set to 2 grids, and the step size for the strength of DMI is set to 0.01. In order to simulate the role of flipping the DMI sign by introducing oxygen in the experiment, the ground state of the alternating-DMI case is re-input as the initial state of the homogeneous-DMI case, as summarized in Fig. 4i–p. To simulate the ground state of the magnetic skyrmionic structures, the iteration times are set to 100,000 or more (Fig. S7).

Micromagnetic simulations

To study the dynamics of various magnetic skyrmionic structures on the DMI-engineered racetrack, the micromagnetic simulations were performed using MuMax3⁶⁴. The magnetization dynamics are described by the Landau–Lifshitz–Gilbert (LLG) eq.:

$$\frac{\partial \mathbf{m}}{\partial t} = -\frac{\gamma}{1+\alpha^2} [\mathbf{m} \times \mathbf{H}_{\text{eff}} + \alpha \mathbf{m} \times (\mathbf{m} \times \mathbf{H}_{\text{eff}})] \quad (12)$$

where \mathbf{m} is the reduced magnetization, γ is the gyromagnetic ratio, α is the dimensionless damping parameter, \mathbf{H}_{eff} is the effective field. The Zhang-Li spin transfer torque takes the form:

$$\boldsymbol{\tau}_{\text{STT}} = \frac{1+\beta\alpha}{1+\alpha^2} \mathbf{m} \times (\mathbf{m} \times (\mathbf{u} \cdot \nabla) \mathbf{m}) + \frac{\beta-\alpha}{1+\alpha^2} \mathbf{m} \times (\mathbf{u} \cdot \nabla) \mathbf{m} \quad (13)$$

$$\mathbf{u} = \frac{\mu_B P}{2e\gamma M_s (1+\beta^2)} \mathbf{j} \quad (14)$$

Where β is the non-adiabaticity of spin-transfer-torque, μ_B is the Bohr magneton, P is electrical current polarization, \mathbf{j} is electrical current density.

The spin-orbit torque takes the form:

$$\boldsymbol{\tau}_{\text{SOT}} = -\gamma \mathbf{m} \times [a_j (\mathbf{m} \times \mathbf{p}) + b_j \mathbf{p}] \quad (15)$$

$$a_j = \left\| \frac{\hbar}{2M_s e} \frac{\alpha_H \mathbf{j}}{d} \right\| \quad (16)$$

$$b_j = \xi a_j \quad (17)$$

$$\mathbf{p} = \text{sign}(\alpha_H) \mathbf{j} \times \mathbf{n} \quad (18)$$

a_j and b_j correspond to the damping-like (Slonczewski–Berger) term and field-like term. \hbar is reduced Planck constant. α_H is spin Hall angle of heavy metal.

For the racetrack investigations, a $512 \times (64,80,110$ in Figs. 5a, b, c and S10 a, b, c, respectively) $\times 1$ grid was used with cell sizes of $1 \times 1 \times 1$ nm. The other simulation parameters are as follows: saturation magnetization $M_s = 0.58$ MA/m, exchange stiffness $A = 15$ pJ/m, perpendicular magnetic anisotropy $K_u = 220$ KJ/m³, interfacial DMI $D_{ij} = 0.5 \sim 3$ mJ/m², damping constant $\alpha = 0.1$, non-adiabaticity of spin-transfer-torque $\beta = 0.2$, electrical current polarization $P = 0.4$, electrical current density $\mathbf{j} = 0.1 \sim 6 \times 10^{12}$ A/m² in spin-transfer-torque simulation, and $\mathbf{j} = 0.1 \sim 4 \times 10^{11}$ A/m² in spin-orbit-torque simulation. Spin Hall angle $\alpha_H = 0.15$. The ratio of field-like term to damping-like term $\xi = -2$. The electrical current density $\mathbf{j} = 1 \times 10^{12}$ A/m² was used in Fig. 5a, b, c and $\mathbf{j} = 5 \times 10^{10}$ A/m² in Fig. S10a, b, c.

Data availability

The data that support the findings of this study are available from the corresponding authors upon request.

References

- Mühlbauer, S. et al. Skyrmion lattice in a chiral magnet. *Science* **323**, 915–919 (2009).
- Yu, X. Z. et al. Real-space observation of a two-dimensional skyrmion crystal. *Nature* **465**, 901–904 (2010).
- Heinze, S. et al. Spontaneous atomic-scale magnetic skyrmion lattice in two dimensions. *Nat. Phys.* **7**, 713–718 (2011).
- Nagaosa, N. & Tokura, Y. Topological properties and dynamics of magnetic skyrmions. *Nat. Nanotechnol.* **8**, 899–911 (2013).
- Braun, H.-B. Topological effects in nanomagnetism: from superparamagnetism to chiral quantum solitons. *Adv. Phys.* **61**, 1–116 (2012).
- Neubauer, A. et al. Topological Hall effect in the A phase of MnSi. *Phys. Rev. Lett.* **102**, 186602 (2009).
- Jiang, W. et al. Direct observation of the skyrmion Hall effect. *Nat. Phys.* **13**, 162–169 (2016).
- Litzius, K. et al. Skyrmion Hall effect revealed by direct time-resolved X-ray microscopy. *Nat. Phys.* **13**, 170–175 (2016).
- Li, J. et al. Tailoring the topology of an artificial magnetic skyrmion. *Nat. Commun.* **5**, 4704 (2014).
- Wild, J. et al. Entropy-limited topological protection of skyrmions. *Sci. Adv.* **3**, e1701704 (2017).
- Sampaio, J., Cros, V., Rohart, S., Thiaville, A. & Fert, A. Nucleation, stability and current-induced motion of isolated magnetic skyrmions in nanostructures. *Nat. Nanotechnol.* **8**, 839–844 (2013).
- Fert, A., Reyren, N. & Cros, V. Magnetic skyrmions: advances in physics and potential applications. *Nat. Rev. Mater.* **2**, 17031 (2017).
- Wiesendanger, R. Nanoscale magnetic skyrmions in metallic films and multilayers: a new twist for spintronics. *Nat. Rev. Mater.* **1**, 16044 (2016).
- Göbel, B., Mertig, I. & Tretiakov, O. A. Beyond skyrmions: review and perspectives of alternative magnetic quasiparticles. *Phys. Rep.* **895**, 1–28 (2021).
- Dzyaloshinsky, I. A thermodynamic theory of “weak” ferromagnetism of antiferromagnetics. *J. Phys. Chem. Solids* **4**, 241–255 (1958).
- Moriya, T. Anisotropic superexchange interaction and weak ferromagnetism. *Phys. Rev.* **120**, 91–98 (1960).
- Nayak, A. K. et al. Magnetic antiskyrmions above room temperature in tetragonal Heusler materials. *Nature* **548**, 561–566 (2017).
- Karube, K. et al. Room-temperature antiskyrmions and sawtooth surface textures in a non-centrosymmetric magnet with S_4 symmetry. *Nat. Mater.* **20**, 335–340 (2021).
- Yu, X. Z. et al. Transformation between meron and skyrmion topological spin textures in a chiral magnet. *Nature* **564**, 95–98 (2018).
- Lin, S.-Z., Saxena, A. & Batista, C. D. Skyrmion fractionalization and merons in chiral magnets with easy-plane anisotropy. *Phys. Rev. B* **91**, 224407 (2015).
- Gao, S. et al. Fractional antiferromagnetic skyrmion lattice induced by anisotropic couplings. *Nature* **586**, 37–41 (2020).
- Ozawa, R., Hayami, S. & Motome, Y. Zero-field skyrmions with a high topological number in itinerant magnets. *Phys. Rev. Lett.* **118**, 147205 (2017).
- Zheng, F. et al. Direct imaging of a zero-field target skyrmion and its polarity switch in a chiral magnetic nanodisk. *Phys. Rev. Lett.* **119**, 197205 (2017).
- Foster, D. et al. Two-dimensional skyrmion bags in liquid crystals and ferromagnets. *Nat. Phys.* **15**, 655–659 (2019).
- Uchida, M., Onose, Y., Matsui, Y. & Tokura, Y. Real-space observation of helical spin order. *Science* **311**, 359–361 (2006).
- Bode, M. et al. Chiral magnetic order at surfaces driven by inversion asymmetry. *Nature* **447**, 190–193 (2007).
- Zhang, X., Zhou, Y. & Ezawa, M. High-topological-number magnetic skyrmions and topologically protected dissipative structure. *Phys. Rev. B* **93**, 024415 (2016).
- Nasr, F., Fillion, C. E., Boulle, O., Béa, H. & Buda-Prejbeanu, L. D. Static and dynamic properties of 1-kink skyrmion in Pt/Co/MgO trilayer. *Phys. Rev. B* **104**, 174441 (2021).
- Staggers, T. L. & Pollard, S. D. Eigenmodes of 1-kink skyrmions in cylindrical magnetic discs. *J. Magn. Magn. Mater.* **591**, 171761 (2024).
- Malozemoff, A. P. & Slonczewski, J. C. Magnetic domain walls in bubble materials: advances in materials and device research (Academic Press, 1979).
- Hassan, M. et al. Dipolar skyrmions and antiskyrmions of arbitrary topological charge at room temperature. *Nat. Phys.* **20**, 615–622 (2024).
- Chen, G. et al. Novel chiral magnetic domain wall structure in Fe/Ni/Cu(001) films. *Phys. Rev. Lett.* **110**, 177204 (2013).
- Rougemaille, N. & Schmid, A. K. Magnetic imaging with spin-polarized low-energy electron microscopy. *Eur. Phys. J. Appl. Phys.* **50**, 20101 (2010).
- Chen, G. & Schmid, A. K. Imaging and tailoring the chirality of domain walls in magnetic films. *Adv. Mat.* **27**, 5738–5743 (2015).
- Legrand, W. et al. Hybrid chiral domain walls and skyrmions in magnetic multilayers. *Sci. Adv.* **4**, eaat0415 (2018).
- Chen, G. et al. Large Dzyaloshinskii–Moriya interaction induced by chemisorbed oxygen on a ferromagnet surface. *Sci. Adv.* **6**, eaba4924 (2020).
- Mentes, T. O., Locatelli, A., Aballe, L. & Bauer, E. Stress induced stripe formation in Pd/W(110). *Phys. Rev. Lett.* **101**, 085701 (2008).
- Altman, M. S., Chung, W. F. & Liu, C. H. LEEM phase contrast. *Surf. Rev. Lett.* **5**, 1129–1141 (1998).
- Chen, G. et al. Ultrasensitive sub-monolayer palladium induced chirality switching and topological evolution of skyrmions. *Nano Lett.* **22**, 6678–6684 (2022).
- Yoshimochi, H. et al. Multistep topological transitions among meron and skyrmion crystals in a centrosymmetric magnet. *Nat. Phys.* **20**, 1001–1008 (2024).
- Jena, J. et al. Evolution and competition between chiral spin textures in nanostripes with D_{2d} symmetry. *Sci. Adv.* **6**, eabc0723 (2020).
- Peng, L. et al. Controlled transformation of skyrmions and antiskyrmions in a non-centrosymmetric magnet. *Nat. Nanotechnol.* **15**, 181–186 (2020).

43. Jena, J. et al. Elliptical Bloch skyrmion chiral twins in an antiskyrmion system. *Nat. Commun.* **11**, 1115 (2020).
 44. Wei, W. et al. Current-controlled topological magnetic transformations in a nanostructured kagome magnet. *Adv. Mater.* **33**, 2101610 (2021).
 45. Khela, M. et al. Laser-induced topological spin switching in a 2D van der Waals magnet. *Nat. Commun.* **14**, 1378 (2023).
 46. Fujishiro, Y. et al. Topological transitions among skyrmion- and hedgehog-lattice states in cubic chiral magnets. *Nat. Commun.* **10**, 1059 (2019).
 47. Bauer, U. et al. Magneto-ionic control of interfacial magnetism. *Nat. Mater.* **14**, 174–181 (2015).
 48. Gilbert, D. A. et al. Controllable positive exchange bias via redox-driven oxygen migration. *Nat. Commun.* **7**, 11050 (2016).
 49. Zheng, F. et al. Experimental observation of chiral magnetic bobbers in B20-type FeGe. *Nat. Nanotechnol.* **13**, 451–455 (2018).
 50. Mulkers, J., Van Waeyenberge, B. & Milošević, M. V. Effects of spatially engineered Dzyaloshinskii-Moriya interaction in ferromagnetic films. *Phys. Rev. B* **95**, 144401 (2017).
 51. Balk, A. L. et al. Simultaneous control of the Dzyaloshinskii-Moriya interaction and magnetic anisotropy in nanomagnetic trilayers. *Phys. Rev. Lett.* **119**, 077205 (2017).
 52. Chen, G. et al. Observation of hydrogen-induced Dzyaloshinskii-Moriya interaction and reversible switching of magnetic chirality. *Phys. Rev. X* **11**, 021015 (2021).
 53. Dai, B. et al. Electric field manipulation of spin chirality and skyrmion dynamic. *Sci. Adv.* **9**, eade6836 (2023).
 54. Gusev, N. S., Sadovnikov, A. V., Nikitov, S. A., Sapozhnikov, M. V. & Udalov, O. G. Manipulation of the Dzyaloshinskii-Moriya interaction in Co/Pt multilayers with strain. *Phys. Rev. Lett.* **124**, 157202 (2020).
 55. Beutier, G. et al. Band filling control of the Dzyaloshinskii-Moriya interaction in weakly ferromagnetic insulators. *Phys. Rev. Lett.* **119**, 167201 (2017).
 56. Li, M. et al. Magnetic domain wall substructures in Pt/Co/Ni/Ir multilayers. *J. Appl. Phys.* **130**, 153903 (2021).
 57. He, Z. et al. Experimental observation of current-driven anti-skyrmion sliding in stripe domains. *Nat. Mat.* **23**, 1048–1054 (2024).
 58. Sinova, J., Valenzuela, S. O., Wunderlich, J., Back, C. H. & Jungwirth, T. Spin Hall effects. *Rev. Mod. Phys.* **87**, 1213–1260 (2015).
 59. Psaroudaki, C. & Panagopoulos, C. Skyrmion qubits: a new class of quantum logic elements based on nanoscale magnetization. *Phys. Rev. Lett.* **127**, 067201 (2021).
 60. Yang, G., Stano, P., Klinovaja, J. & Loss, D. Majorana bound states in magnetic skyrmions. *Phys. Rev. B* **93**, 224505 (2016).
 61. Hervé, M. et al. Stabilizing spin spirals and isolated skyrmions at low magnetic field exploiting vanishing magnetic anisotropy. *Nat. Commun.* **9**, 1015 (2018).
 62. Kortan, A. R. & Park, R. L. Phase diagram of oxygen chemisorbed on nickel (111). *Phys. Rev. B* **23**, 6340–6347 (1981).
 63. Kwon, H. Y. & Won, C. Effects of Dzyaloshinskii-Moriya interaction on magnetic stripe domains. *J. Magn. Magn. Mater.* **351**, 8–15 (2014).
 64. Vansteenkiste, A. et al. The design and verification of MuMax3. *AIP Adv.* **4**, 107133 (2014).
- (NRF) funded by the Korean Government (NRF-2021R1C1C2093113) and the Korea Institute of Science and Technology Institutional Program (2E33421). Y.Z.W. acknowledges support by the National Natural Science Foundation of China (Grant No. 11974079) and the Shanghai Municipal Science and Technology Major Project (Grant No. 2019SHZDZX01). K.L. acknowledges support from the US-NSF (DMR-2005108). C.W. acknowledges support by the National Research Foundation of Korea (NRF) funded by the Korean Government (NRF-2023R1A2C1006050). Work at the Molecular Foundry was supported by the Office of Science, Office of Basic Energy Sciences, of the US Department of Energy under contract no. DE-AC02-05CH11231 (A.K.S.).

Author contributions

G.C. conceived the study. G.C. and H.D. supervised the project and SPLEEM facility. H.N. carried out the experiments and analyzed the data. H.G.Y., H.Y.K., and C.W. performed Monte-Carlo simulations. H.Y.K. and C.W. constructed the analytical model. H.N. and H.Z. performed the micromagnetic simulations. H.N., H.G.Y., H.Y.K., Z.C., S.F., H.Z., B.M., L.S., Y.W., A.K.S., K.L., C.W., H.D., and G.C. discussed and interpreted the results. H.N., H.D., and G.C. prepared the manuscript. All authors commented on the manuscript.

Competing interests

The authors declare no competing interests.

Additional information

Supplementary information The online version contains supplementary material available at <https://doi.org/10.1038/s41467-025-58529-4>.

Correspondence and requests for materials should be addressed to Haifeng Ding or Gong Chen.

Peer review information *Nature Communications* thanks Shawn Pollard, Myoung-Woo Yoo, and the other anonymous reviewer(s) for their contribution to the peer review of this work. A peer review file is available.

Reprints and permissions information is available at <http://www.nature.com/reprints>

Publisher's note Springer Nature remains neutral with regard to jurisdictional claims in published maps and institutional affiliations.

Open Access This article is licensed under a Creative Commons Attribution-NonCommercial-NoDerivatives 4.0 International License, which permits any non-commercial use, sharing, distribution and reproduction in any medium or format, as long as you give appropriate credit to the original author(s) and the source, provide a link to the Creative Commons licence, and indicate if you modified the licensed material. You do not have permission under this licence to share adapted material derived from this article or parts of it. The images or other third party material in this article are included in the article's Creative Commons licence, unless indicated otherwise in a credit line to the material. If material is not included in the article's Creative Commons licence and your intended use is not permitted by statutory regulation or exceeds the permitted use, you will need to obtain permission directly from the copyright holder. To view a copy of this licence, visit <http://creativecommons.org/licenses/by-nc-nd/4.0/>.

© The Author(s) 2025

Acknowledgements

We are grateful to Professor Tianping Ma for insightful discussions. This work has been supported by the National Key R&D Program of China (Grant Nos. 2024YFA1408501, 2022YFA1403601, and 2023YFC2410501) and the National Natural Science Foundation of China (Grants Nos. 12374113, 12474059, 12274204, 12274203, and 12241402). H.Y.K. acknowledges support by the National Research Foundation of Korea